Aerosol Science and Technology, 39:206–221, 2005

ISSN: 0278-6826 print / 1521-7388 online
DOI: 10.1080/027868290913988

A Continuous-Flow Streamwise Thermal-Gradient CCN Chamber for Atmospheric Measurements

G. C. Roberts

Center for Atmospheric Sciences, Scripps Institution of Oceanography, La Jolla, California, USA

A. Nenes

Schools of Earth and Atmospheric Science and Chemical and Biomolecular Engineering, Georgia Institute of Technology, Atlanta, Georgia, USA

We have addressed the need for improved measurements of cloud condensation nuclei (CCN) by developing a continuous-flow instrument that provides in situ measurements of CCN. The design presented in this article can operate between 0.1 and 3% supersaturation, at sampling rates sufficient for airborne operation. The design constitutes a cylindrical continuous-flow thermal-gradient diffusion chamber employing a novel technique of generating a supersaturation: by establishing a constant streamwise temperature gradient so that the difference in water vapor and thermal diffusivity yield a quasi-uniform centerline supersaturation. Our design maximizes the growth rate of activated droplets, thereby enhancing the performance of the instrument. The temperature gradient and the flow through the column control the supersaturation and may be modified to retrieve CCN spectra.

The principle of the CCN instrument was validated in controlled laboratory experiments at different operating conditions using a monodisperse aerosols with known composition and size. These experiments yield sharp activation curves, even for those kinetically limited particles that have not exceeded their critical diameter. The performance of the CCN instrument was also assessed using polydisperse laboratory-generated aerosol of known composition and size distributions similar to ambient particulate matter. In all tests, the measured CCN concentrations compared well with predicted values and highlight the instrument's ability to measure CCN at various size distributions.

The full potential of the new design has yet to be explored; however, model simulations suggest that direct measurements in the climatically important range of supersaturations of less than 0.1% (certainly down to 0.07%) are possible. The new instrument clearly offers a unique level of design simplicity, robustness, and flexilibity (temperature control, large range of supersaturations without flow reversal, and multiple configurations for same supersaturation) necessary for atmospheric studies.

INTRODUCTION

The largest uncertainty in anthropogenic climate change stems from aerosol–cloud interactions and their effect on the atmospheric radiative balance and hydrological cycle (Houghton et al. 2001). Aerosols are precursors to cloud droplets, and their size, concentration, and affinity to water vapor directly influence cloud microphysical and radiative properties. Models and field observations (e.g., Kaufman et al. 1998; Ramanathan et al. 2001; Raes et al. 2000) have shown that the presence of anthropogenic aerosols can increase cloud droplet concentrations in low-level clouds and exert a climatic cooling effect by enhancing cloud albedo (Twomey 1977; Charlson et al. 1992) and decreasing precipitation efficiency (Albrecht 1989; Rosenfeld 1999). Establishing a quantitative relationship between aerosols and cloud properties is a requirement for understanding anthropogenic climate change, but it has not been accomplished to date.

Measurements of those particles that can become cloud droplets (or cloud condensation nuclei, CCN) are essential for providing a quantitative link between cloud microphysics and the physicochemical properties of aerosol. Observations are typically represented as number of CCN as a function of water vapor supersaturation (otherwise known as *supersaturation spectrum*). This is done because each CCN particle requires a minimum water vapor supersaturation, or critical supersaturation, S_c, to convert into a cloud droplet. When exposed to supersaturations larger than S_c, particles must grow to a *critical diameter*, $D_{pc,}$ before reaching a mode of unstable (unconstrained) growth, otherwise known as *activation*. Upon activation, water vapor spontaneously condenses onto CCN, which quickly

Received 8 July 2004; accepted 3 December 2004.

The authors express their appreciation to Dr. C. F. Rogers for the informative discussions and for shedding light on their earlier efforts. We thank Dave Malmberg at the Marine Science Development Shop at Scripps Institution of Oceanography and Frank Helleis at Max Planck Institute for Chemistry in Mainz, Germany for their assistance in constructing the CCN counter. This project was made possible through the National Science Foundation (grant no. NSF ATM 02-01946). We also acknowledge the thoughtful comments of an anonymous reviewer.

Address correspondence to G. C. Roberts, Center for Atmospheric Sciences, Scripps Institution of Oceanography, (9500 Gilman Dr. #0239, La Jolla, California 92093, USA. E-mail: greg@fiji.ucsd.edu

grow to a large size (ca. 10 μm in ambient clouds) limited only by diffusional kinetics and the availability of water vapor. S_c and D_{pc} are a strong function of dry particle size and chemical composition.

Instruments that measure CCN concentrations at a single supersaturation have existed for decades. The thermal gradient diffusion cloud chamber (or *static diffusion chamber*) is perhaps the most widely used since its introduction by Twomey (1963). A known supersaturation profile develops in the chamber between two wet parallel plates. Once activated, aerosol particles grow and gravitationally settle out of the illuminated sample volume. To obtain CCN concentrations, the chamber must be flushed and isolated to allow the supersaturation profile to develop. Therefore, a single measurement requires at least 20 s at a particular supersaturation. The lowest supersaturation at which CCN can be measured in static diffusion chambers is greater than 0.2% (Sinnarwalla and Alofs 1973; Nenes et al. 2001a) due to insufficient time for droplet growth, and this is not low enough to match supersaturations found in some marine stratus clouds. Calibration of the static diffusion chamber is obtained empirically and has been investigated by several groups (Lala and Jiusto 1977; Bartlett and Ayers 1981; Oliveira and Vali 1995; Delene et al. 1998). To overcome some of the limitations of the static thermal-gradient chamber, several variations of the continuous-flow parallel plate thermal diffusion chamber were developed (e.g., Sinnarwalla and Alofs 1973; Fukuta and Saxena 1979; Hudson 1989). The continuous sample flow eliminates batch sampling; however, they are limited to supersaturations larger than 0.1% due to long growth times and thermophoretic/diffusiophoretic forces (Sinnarwalla and Alofs 1973; Nenes et al. 2001a).

Hudson (1989) employed an extension of the continuous-flow thermal chamber technique to develop a CCN spectrometer with a reported range of supersaturations between 0.01 and 1%. Chuang et al. (2000) used an alternating-gradient technique to construct a continuous flow CCN spectrometer with cylindrical symmetry by combining concepts from Hudson (1989) and Hoppel (1979). Both of these instruments operate on the requirement that particles with the same critical supersaturation will exhibit the same growth behavior when exposed to identical supersaturation fields. In practice, however, this is not the case, particularly for carbonaceous aerosol containing surfactants and slightly soluble material that changes the Köhler curves and modifies growth behavior. Many studies clearly show this; for example, Shulman et al. (1996) and Facchini et al. (1999, 2000) show that organics change the droplet's surface characteristics and hence influence their growth rates. More recent modeling and experimental studies (i.e., Hegg et al. 2001; Feingold et al. 2002; Chuang et al. 2003; Shantz et al. 2003) suggest that the difference in growth rates between soluble inorganic and organic particles has important implications for cloud microphysical studies; however, unambiguous experimental evidence of such effects on scales relevant for global aerosol still remains to be determined. Nonetheless, differences in the growth kinetics between CCN with the same critical supersaturation compromises the usefulness of the methodology assumed by the aforementioned CCN spectrometers. A thorough review and assessment of the performance of various CCN instruments is presented by Nenes et al. (2001a).

Constructing a CCN instrument that is widely applicable (particularly for airborne measurements) must satisfy stringent constraints of size, weight, and power consumption. In addition, the high aircraft velocity requires rapid measurements to quantify CCN within an adequate temporal and spatial resolution for cloud studies. CCN instruments have been deployed in aircraft since their conception (e.g., Twomey and Wojciechowski 1969), and recently smaller, autonomous CCN instruments have been developed for research aircraft. Delene et al. (1998) deployed a static thermal-gradient chamber on tethered balloons to obtain vertical profiles of CCN at 1% supersaturation within the troposphere. However, one sample every 20 s (a constraint of static diffusion chambers) limits the instrument's deployment on a fast platform or in variable atmospheric conditions. The continuous flow alternating-gradient CCN instrument developed by Chuang et al. (2000) was developed for airborne deployment and may be used as a single supersaturation instrument. However, the oscillations in supersaturation along the column's axis slow down or even reverse particle growth, so less of the instrument is utilized for particle growth (Nenes et al. 2001a). Our instrument combines important features of continuous-flow parallel plate diffusion chambers (e.g., Sinnarwalla and Alofs 1973; Fukuta and Saxena 1979; Hudson 1989) and cylindrical diffusion chambers (e.g., Hoppel et al. 1979; Chuang et al. 2000)—these features include continuous flow for high resolution measurements; exposure of a particle to a constant supersaturation, which maximizes particle growth; and cylindrical symmetry that minimizes buoyancy effects, instrument size, thermo- and diffusiophoretic forces, and logistical issues (i.e., column wetting, droplet detection, temperature control).

CCN measurements are among the most demanding in atmospheric sciences; obstacles in instrument development and data interpretation pose inherent problems that originate from the low water vapor supersaturation that exists in clouds. Developing a technique that generates ambient supersaturations in a controlled manner, within a small package that responds quickly to ambient changes (necessary conditions for in situ aircraft measurements), has proven to be challenging. In addition, instrument development in this field is often empirical, often leading to measurements with unquantified uncertainty. Future studies on aerosol–cloud–climate interactions require a serious effort to provide adequate instrumentation to bridge the gap between aerosols and clouds. Significant improvements in the measurement techniques are needed, and this development constitutes an important step in this direction.

BACKGROUND

The ability of an aerosol particle to serve as a CCN depends on its size and chemical composition. The ratio of equilibrium water vapor pressure at the surface of the droplet to that of pure water over a flat plane is the equilibrium saturation ratio, $S_R{}^{eq}$, and in its simplest form it is described by "classical" Köhler theory (Köhler 1936; Pruppacher and Klett 1997; Seinfeld and Pandis 1998). In its simplest form (e.g., Equation (10)), two competing terms describe $S_R{}^{eq}$; the surface tension term (i.e., the Kelvin effect) accounts for enhanced vapor pressure due to droplet curvature and scales with inverse diameter, $D_p{}^{-1}$, and the dissolved solute term (i.e., the Raoult effect) depresses the water vapor pressure at the droplet surface and scales with $D_p{}^{-3}$. The maximum $S_R{}^{eq}$ of the Köhler curve defines the critical supersaturation, S_c, and occurs at the droplet's critical diameter, D_{pc}. The droplet can be in stable equilibrium with its environment when its diameter is less than D_{pc}. However, when the particle is exposed to a supersaturation $S > S_c$ and $D_p > D_{pc}$, the particle activates and continues to grow as long as the surrounding water vapor pressure in the air is greater than the equilibrium vapor pressure of the solution droplet (this is mostly true for ambient clouds, except for cases of very high CCN concentrations; e.g., Nenes et al. 2001b).

The shape of the Köhler curve controls droplet growth and is readily modified by surfactants and slightly soluble constituents in ambient aerosols. The presence of surface-active substances from the water-soluble organic carbon (WSOC; in particular, humic-like substances, HULIS), has a significant influence on the equilibrium vapor pressure by reducing the droplet's surface tension (Shulman et al. 1996; Facchini et al. 2000; Mircea et al. 2002), which lowers S_c and facilitates droplet growth. Slightly soluble compounds and soluble gases also affect the shape of the Köhler curve (Shulman et al. 1996; Laaksonen et al. 1998) and may even allow the occurrence of stable, unactivated droplets of 20 μm diameter in realistic, albeit polluted, conditions. It is possible that the presence of organic surfactants (so-called film-forming compounds) may also affect the rate of water vapor condensation and thus potentially have a strong effect on cloud droplet number and dispersion (Feingold and Chuang 2002; Nenes et al. 2002; Chuang 2003). Such "chemical effects" on the Köhler curve result in different droplet growth kinetics and may impose challenges in distinguishing activated from unactivated droplets, as well as mandating redefinition of what constitutes a CCN. Nonetheless, interpreting measurements from CCN instruments requires an understanding of these nuances and proper assessment of their importance in light of aerosol–cloud interactions.

DESCRIPTION OF THE CONTINUOUS-FLOW STREAMWISE THERMAL-GRADIENT DIFFUSION CHAMBER

Before the inception of the new design, we initially intended to adopt the single-supersaturation alternating-temperature concept introduced by Hoppel et al. (1979), but within a axisymmetric flow geometry (i.e., a design similar to that of Chuang et al. 2000). The disadvantage of this methodology is that the supersaturation profile oscillates in the axial direction (Figure 1a); hence, the droplets are exposed to a range of supersaturations that introduce measurement uncertainty and even limit droplet growth (the instrument may be subsaturated at certain points, thus evaporating the droplets). Simulations of the alternating-gradient technique achieved only marginal performance using a fully coupled model developed by Nenes et al. (2001a). Hence, while trying to improve the alternating-temperature design, successive sections were heated slightly warmer than previous ones to prevent the airstream from equilibrating in a single heated section. This pattern was extended along the column, resulting in a nearly constant centerline supersaturation with small oscillations about the mean. Extending this concept to smaller simulated heated sections and a more uniform increase temperature resulted in a linear temperature gradient and a smooth, quasi-uniform centerline supersaturation (Figure 1b) that allowed for continuous growth of the droplets throughout the instrument.

We then conceived the simplest possible implementation; the heated sections were replaced with a continuous temperature gradient achieved by conduction along a conductive cylindrical wall (Figure 2). This change not only improves the performance of the CCN instrument by stabilizing the supersaturation profile, but it also vastly simplifies the design. Instead of controlling the wall temperatures for 14 (or more) sections as in Chuang et al. (2000), the desired temperature profile may be established by regulating the temperature at each end of the column. Only after the successful development, characterization of the prototype, and deployment of the instrument on an aircraft did we become aware of the work by Rogers and Squires (1977). Patrick Squires explored this concept four decades ago (Rogers, personal communication); however, a broad droplet spectrum observed by the optical particle counter impeded further development. Our simulations suggest their apparatus could exhibit a nonlinear temperature profile and flow instability near the wetted surface in certain conditions (Section 6). Our design and implementation ensures that such issues never appear. In the following paragraphs we describe the operation of the new CCN instrument by discussing the main components (shown in Figure 2), and then we proceed with a thorough theoretical description of the instrument in the sections "Theory of Operation" and "Fully Coupled Instrument Model," and experimental validation in the final two sections, "Instrument Performance and Design Constraints" and "Instrument Validation." We advise the reader that several improved versions of this instrument have since been constructed; we describe the original device in this manuscript.

Temperature Control

A vertical cylindrical column in Figure 2 constitutes the CCN growth chamber. The column's inner surface is

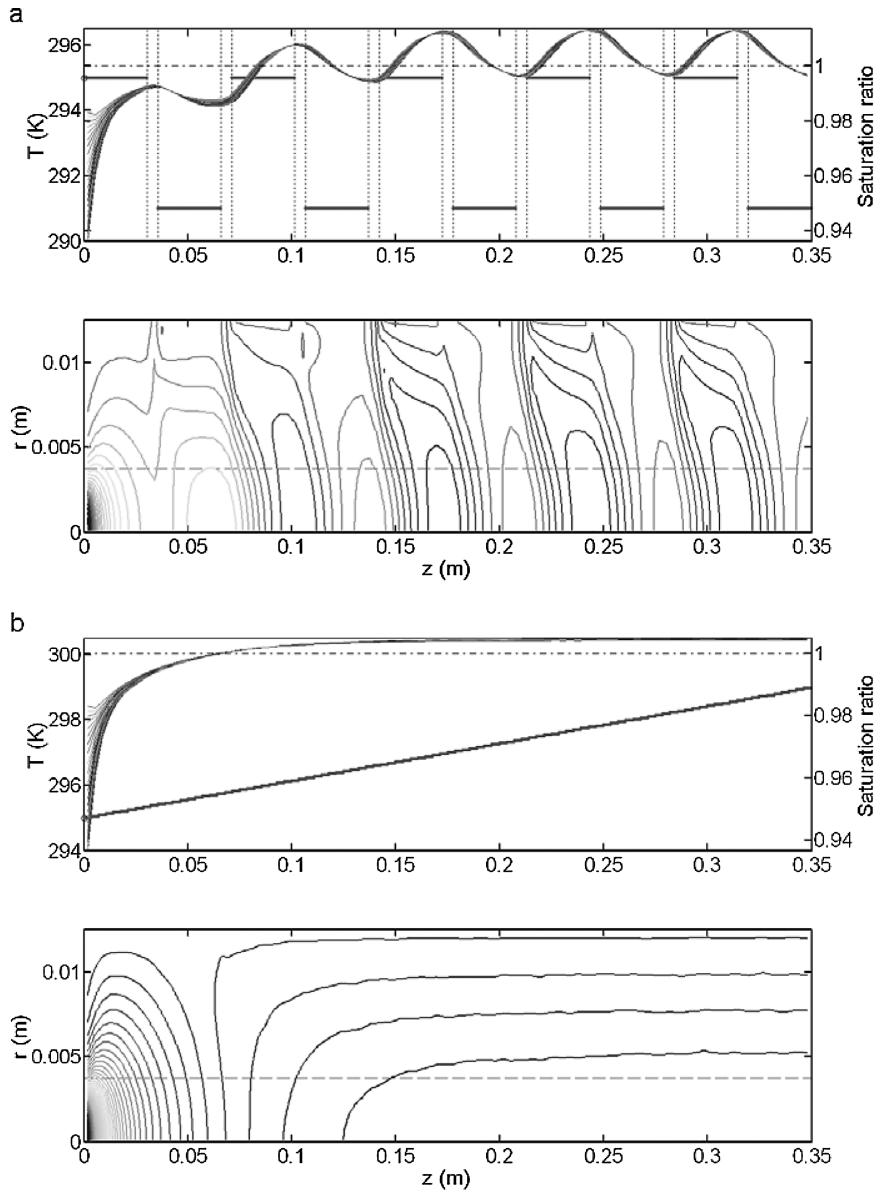

FIG. 1. (a) The alternating gradient technique for repeating hot/cold sections in cylindrical symmetry. The upper graph shows the alternating temperature gradient (horizontal bars) and the development of the supersaturation profile near the centerline of the chamber (multiple sinusoidal lines). Notice that the minimum saturation ratio briefly drops below 1 (<0% supersaturation) just after the cold sections. Droplets momentarily evaporate during this period. The lower graph illustrates the contours of the supersaturation profile in the radial, r, and streamwise, z, dimensions. The centerline is at $r = 0$. The dashed line approximates the aerosol boundary in the column. (b) The linear thermal-gradient technique in cylindrical symmetry. The upper graph shows the linear temperature gradient (straight line) and the development of the uniform supersaturation profile near the centerline of the chamber. Notice that unlike (a), the supersaturation is always positive (or $S_R > 1$) throughout most of the instrument. The lower graph illustrates the contours of the supersaturation profile in the radial and streamwise dimensions. The centerline is at $r = 0$. The dashed line approximates the aerosol boundary in the column.

maintained wet and exposed to an increasing temperature gradient along the streamwise vertical axis. The dimensions of the column are 10.9 mm radius and 360 mm long and wall thickness of 8 mm. To generate a nearly linear temperature gradient, the column's walls must be sufficiently thick so that heat transfer in the streamwise axis (within the wall) is much greater than the convective heat losses to the sample flow and through the insulation surrounding the column. Four thermal electric coolers (TECs) surround the column on each end to maintain the prescribed temperature (and temperature gradient). The TECs are mounted on each side of a 34 mm × 34 mm × 38 mm block that securely fits around the column, and heat-conductive silicon paste between the TECs, block, and the column ensures proper heat transfer. Temperature measurements are made at

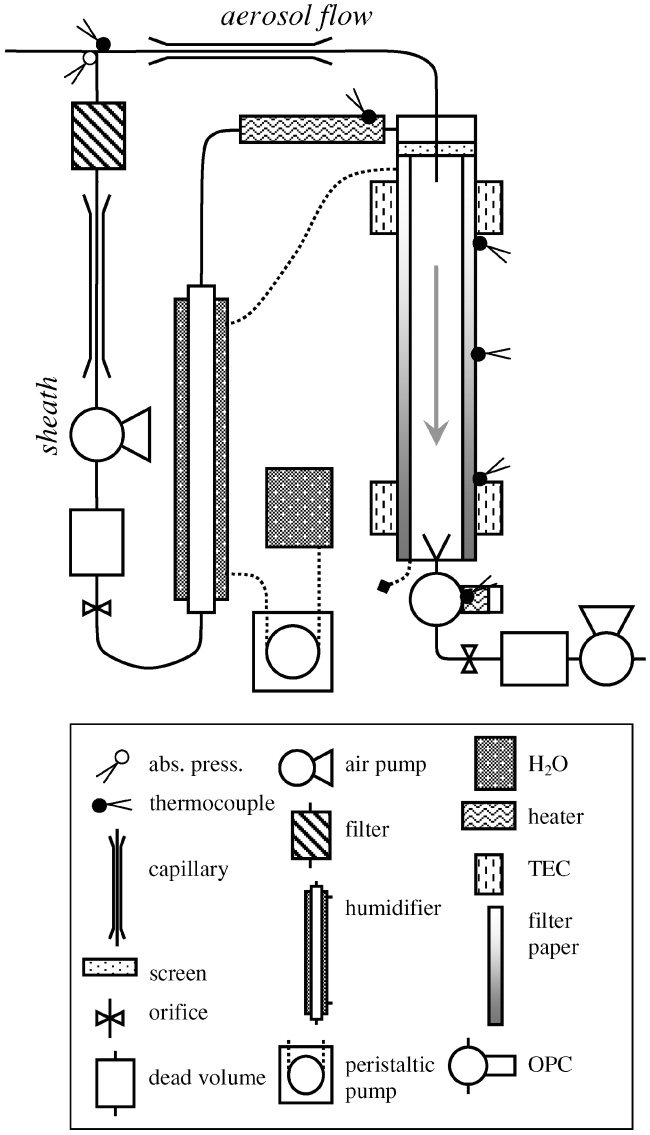

FIG. 2. Operational and flow schematic of the streamwise thermal gradient CCN instrument.

six locations along the column (shown in Figure 2) with type E thermocouples (subsequently replaced with resistance temperature detectors (RTDs) due to higher precision and lower noise).

The top column temperature, T_c, operates slightly above the ambient temperature surrounding the instrument; the absolute value is not critical for the overall operation (section "Instrument Performance and Design Constraints") as long as the growth chamber is sufficiently insulated to maintain the linear temperature profile. The sheath flow is actively heated with resistance wire to slightly above T_c (ca. 1 K) to prevent inadvertent activation of particles in the entrance portion of the column where the sample and sheath flows rejoin. Another resistance wire heater keeps the optical particle counter (OPC) slightly warmer than the bottom-column temperature, T_h, to prevent condensation of water vapor on the optics and detector. The residence time of the activated drops within the OPC is too small to be affected by the raise in temperature. The OPC is heated to ca. 2 K above T_h during normal operation.

Flow Control

The schematic in Figure 2 also shows the flow system of the CCN instrument. A Y-shaped inlet splits the sample airstream into separate aerosol and sheath flows while minimizing impaction losses. The aerosol sample flows through a stainless-steel capillary, while a differential pressure sensor (5″ H_2O full-scale, temperature-compensated Honeywell sensor) across the capillary measures the volumetric flow. The differential pressure has been calibrated to volumetric flow using an inline bubble flow meter. Electrically conductive tubing for the sample flow is made as short as possible to minimize diffusion losses, which have been calculated to be less than 3% for 27 nm diameter particles (1% S_c for ammonium sulfate, $(NH_4)_2SO_4$ particles). Impaction losses are negligible for aerosol that is less than 10 μm diameter (0.00014% S_c for $(NH_4)_2SO_4$ particles).

The sheath flow is directed through a total aerosol filter, capillary flow meter, pump, humidifier, and heater before being introduced into the headspace above the wetted column. A mesh separates the headspace and the wetted column, and via a slight pressure gradient it uniformly distributes the aerosol-free humidified sheath flow. Before rejoining with the aerosol flow, the sheath flow is allowed to achieve fully developed annular flow. This annular configuration keeps the sample in a region of nearly uniform supersaturation in the centerline region to minimize wall losses. We nominally use a 10-to-1 volumetric ratio for the sheath and aerosol flow rates, also referred to as a sheath-to-aerosol ratio (SAR) of 10. We tested the configuration with SARs between 5 and 20, which allows us to optimize the flow rate depending on the CCN number concentration. Small SARs can be used for low concentrations to achieve sufficient counting statistics, while larger SARs are useful in regions of high aerosol concentrations to minimize coincidence losses in the OPC.

After the sheath and aerosol flows have been rejoined, the air then flows vertically downward through the chamber and is exposed to the temperature gradient along the wetted surface. Particles with a critical supersaturation less than the centerline S activate and grow into droplets. The length of the column and flow rate must be optimized to achieve sufficiently large particles to separate activated from unactivated (*interstitial*) droplets. A collector cone at the bottom of the chamber focuses the sample and sheath flows and introduces the airstream into the OPC. The cone has an included angle of 30° (i.e., 15° from the flow axis), and its opening is slightly smaller than the chamber diameter so that excess water drains along the walls without flooding the OPC. A pump downstream of the OPC pulls the airstream through the instrument. Dead volumes and orifices are placed between each of the diaphragm

pumps and the column to eliminate pressure oscillations in the growth chamber. Software controls the pumps'speeds to maintain a constant flow and SAR.

Optical Particle Counter

An optical particle counter (OPC) employs standard light-scattering techniques to detect droplets at the outlet of the growth column. The OPC (Model 9012) is available commercially through MetOne Intruments, Inc. (Grants Pass, OR, USA) and uses a 780 nm, 30 mW wavelength photodiode laser. The light enters the scattering chamber through a cylindrical focal-length lens, which focuses the beam to a 0.1 mm thick sample volume at about 1 mm from the end of the inlet. Measured pulses are typically 10 μs. A gold surface elliptical mirror is mounted opposite the detector about 10 mm from the scattering volume and reflects a 100 degree solid angle fraction of the scattered light to the detector. The detector is a 3.8 mm $\times$ 3.8 mm silicon diode mounted about 15 mm from the scattering volume, perpendicular to the laser beam. The detector also receives an insignificant direct 15° solid-angle fraction of the scattered light. The electronics processor from MetOne counts and sizes the detector output into six size-selectable bins, which we have chosen to be 0.5, 0.7, 1.0, 2.0, 3.0, and 6.0 μm. The size cutoffs of the bins have been calibrated at MetOne, and the smallest detectable particle size is 0.3 μm. The number count of particles with diameters greater than the bin size cutoff is exported via RS-232 communication at 1 Hz.

A collection cone has been attached to the OPC to bring the sample into the scattering volume with minimal bias to the droplet size spectra. Those droplets larger than 1.0 μm are considered CCN and comprise the CCN concentration. The droplet size cutoff imposes constraints on the operational limit of instrument and is discussed in further detail in the section "Optical detection constraints." The performance of the OPC has been assessed and coincidence errors are not significant for most CCN measurements (see section "Instrument Validation").

Column Wetting

Two layers of filter paper (Whatman 1) are used to maintain a wetted inner surface of the chamber. A reservoir below the column supplies the water to the peristaltic pump, which pushes the water upwards, through the Nafion humidifier (Perma-Pur Inc.) and into the top of the column. The humidifier conditions the sheath flow before it enters the column. Water is introduced through a radial band of small holes at top of the column for uniform distribution around the filter paper. The column is manually rewetted, and excess water is periodically drained from the bottom of the column.

Electronics Interface

The electronic interface for the CCN instruments has been designed for automatic aquisition and control of previously described features of the instrument. Its main parts are a industry standard $\times$86-compatible NEC V25 microcontroller, an interface backplane, and various extension boards, which interface the process controller to the various components. Because of its high modularity, the system is easily scaleable and is therefore adaptable to the development of the CCN instrument. The interface is assembled in a standard 19$''$ rack-mounted container. Seven analog-to-digital (A/D) input channels (16 bit resolution, low noise, 50 Hz suppression) collect temperature and differential pressure measurements. Eight digitial-to-analog (D/A) channels (12 bit, low noise, 50 Hz suppression) control the thermal electric coolers, pumps, and resistance heaters. Data storage capabilities on PCMCIA media storage provide ample storage space, and a RS-232 interface is also available to connect to secondary hosts. An integrated menu-driven LCD and six-key user interface provide an efficient, user-friendly interface for controlling various parameters and assessing the performance of the instrument.

THEORY OF OPERATION

This section focuses on illustrating the principles for developing the water vapor supersaturation at any point within the chamber. The underlying mechanism of generating a supersaturation relies on the difference in heat and mass diffusion (e.g., 0.21 cm^2 s^{-1} versus 0.25 cm^2 s^{-1} at 294 K, 1 atm, respectively), which is consequence of the low concentration and molar mass of water vapor with respect to air. Water molecules, being lighter than N_2 and O_2, diffuse more quickly in air than heat because the latter is governed by the collisions between (on average slower) air molecules.

A simple scaling analysis can be employed to explore the relationship between the main parameters affecting instrument supersaturation. Heat and mass both diffuse from the walls of the instrument inward; the timescale needed for mass and heat to reach the instrument centerline is $\tau_C = R^2/D_v$ and $\tau_T = R^2/\alpha$, respectively (Incropera and DeWitt 1990), where R is the column radius, D_v is the diffusivity of water vapor, and α is the diffusivity of heat. If the air flow rate is Q, with an average velocity of $V = Q/\pi R^2$, then heat from the wall travels propagates, $x_T = V\tau_T = Q/_{\pi\alpha}$, in the axial direction before reaching the centerline (a factor of 5/3 should be introduced if the parabolic velocity profile is considered; this, however, would not seriously affect our analysis and is omitted for simplicity). Similarly, mass travels an axial distance, $x_C = Q/_{\pi D_v}$. Therefore, points along the symmetry axis will have (to first order) the wall temperature and water vapor concentration at a distance x_T and x_C upwind, respectively (Figure 3), i.e., $T(0,z) \approx T(R, z - x_T)$, and $P_{H_2O}(0,z) \approx P_{H_2O}(R, z - x_c)$. Furthermore, water vapor is saturated at the walls, hence $P_{H_2O}(R, z - x_c) = P^o_{H_2O}(R, z - x_c)$ and $P_{H_2O}(0,z) \approx P^o_{H_2O}(R, z - x_c)$. The saturation ratio at the

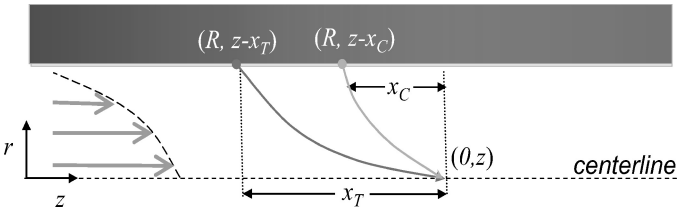

FIG. 3. Schematic of the geometry used for the analysis of the section "Theory of Operation."

centerline, $S_R(z) = \frac{P_{H_2O}}{P^o_{H_2O}(T)}$, will then be

$$S_R(z) = \frac{P_{H_2O}(0,z)}{P^o_{H_2O}(T(0,z))} \approx \frac{P^o_{H_2O}(R, z - x_C)}{P^o_{H_2O}(R, z - x_T)} \qquad [1]$$

The temperature profile along the wall, $T(R, z)$, varies linearly with z as the instrument operates on the principle of a constant axial thermal-gradient. Since $x_C < x_T$, the instrument centerline is supersaturated (once the thermal, water vapor, and momentum profiles have developed). Substitution of a relationship between x_C, x_T, wall temperature gradient, and vapor pressure into Equation (1) will then give an explicit relationship between supersaturation and instrument parameters.

The equilibrium vapor pressure, $P^o_{H_2O}$, increases with temperature according to the Clausius-Clapeyron equation:

$$\frac{P^o_{H_2O}(T_2)}{P^o_{H_2O}(T_1)} = \exp\left[\frac{\Delta H_v}{R_g}\left(\frac{1}{T_1} - \frac{1}{T_2}\right)\right] = \exp\left[\frac{\Delta H_v}{R_g}\frac{(T_2 - T_1)}{T_1 T_2}\right], \qquad [2]$$

where ΔH_v is the enthalpy of evaporation of water and R_g is the universal gas constant. For small temperature differences, $T_1 T_2 \approx T_1^2$ and the exponential can be approximated with a first-order Taylor series expansion:

$$\frac{P^o_{H_2O}(T_2)}{P^o_{H_2O}(T_1)} \approx 1 + \frac{\Delta H_v}{R_g}\frac{(T_2 - T_1)}{T_1^2} \qquad [3]$$

Substitution of Equation (3) into Equation (1) gives

$$S_R(z) = \frac{P^o_{H_2O}(T(R, z - x_C))}{P^o_{H_2O}(T(R, z - x_T))} \approx 1 + \frac{\Delta H_v}{R_g}\frac{\Delta T}{(T(R, z - x_T))^2}, \qquad [4]$$

where $\Delta T = T(R, z - x_C) - T(R, z - x_T)$. Since the temperature gradient, G, is constant, $\Delta T = G(x_T - x_C)$, where $x_T - x_C$ can be calculated from the residence and diffusional timescales:

$$x_T - x_C = (\tau_T - \tau_C)V = VR^2\left(\frac{1}{\alpha} - \frac{1}{D_v}\right). \qquad [5]$$

With the above, and since $T(R, z - x_T) = T(R, z) - Gx_T = T(R, z) - G\frac{R^2 V}{\alpha}$, the instrument centerline supersaturation, $S = S_R - 1$, can be expressed as:

$$S(z) = \frac{\Delta H_v}{R_g}\frac{GVR^2}{\left(T(R,z) - G\frac{R^2V}{\alpha}\right)^2}\left(\frac{1}{\alpha} - \frac{1}{D_v}\right) = \frac{\Delta H_v}{\pi R_g}\frac{GQ}{\left(T(R,z) - \frac{1}{\pi}\frac{GQ}{\alpha}\right)^2}\left(\frac{1}{\alpha} - \frac{1}{D_v}\right). \qquad [6]$$

Equation (6) gives the functional dependence of centerline supersaturation with respect to the operational (i.e., G, Q) and other relevant thermophysical (i.e., α, D_v, ΔH_v) parameters. If the temperature drop along the length of the column is small compared to the inlet temperature, then $T(R, z) - \frac{1}{\pi}GQ/\alpha \approx const.$, and according to Equation (6) $S(z) \approx const.$ Under such conditions, the instrument operates as a single supersaturation CCN counter. In reality, since the denominator of Equation (6) always increases with z, $S(z)$ should drop with roughly a z^{-2} dependence (if α, D_v do not vary considerably and if the constant wall temperature gradient is maintained); selecting the right combination of G and Q, however, would give minimal drop for a wide range of centerline supersaturations.

FULLY-COUPLED INSTRUMENT MODEL

To test the feasibility and performance of the new instrument, design, flow, heat, and mass transfer within the growth chamber have all been numerically modeled to determine the temperature, water vapor, and supersaturation distributions as a function of position and time. Laminar flow conditions are required for proper instrument operation; the Reynolds number is thus small (typically below 50). Particle activation and growth are simulated by tracking individual CCN as they flow through the instrument. The equations used to describe aerosol particle growth are first given in the next section, followed by the general form of the gas-phase equations. Finally, the appropriate boundary conditions and instrument-specific relations for each parameter are given.

Aerosol Growth

The rate of change of droplet size for each of the particles is calculated from the diffusional growth equation (Seinfeld and Pandis 1998):

$$D_p\frac{dD_p}{dt} = \frac{\left(S - S_R^{eq}\right)}{\frac{\rho_w R_g T}{4P^o_{H_2O}D'_v M_w} + \frac{\Delta H_v \rho_w}{4k'_a T}\left(\frac{\Delta H_v \rho_w}{TR_g} - 1\right)}, \qquad [7]$$

where D_p is the particle diameter, $S = P_{H_2O}/P^o_{H_2O} - 1$ is the local supersaturation, S_v^{eq} is the equilibrium supersaturation of the droplet, ρ_w is the water density, M_w is the molar mass of water, D'_v is the diffusivity of water vapor in air modified for

noncontinuum effects (Fukuta and Walter 1970),

$$D_v' = \frac{D_v}{1 + \frac{2D_v}{\alpha D_p}\sqrt{\frac{2\pi M_w}{R_g T}}}, \quad [8]$$

where D_v is the diffusivity of water vapor in air, a_c is the condensation coefficient, $k\prime_a$ is the thermal conductivity of air modified for noncontinuum effects,

$$k_a' = \frac{k_a}{1 + \frac{2k_a}{\alpha_T D_p \rho_a c_p}\sqrt{\frac{2\pi M_a}{R_g T}}}, \quad [9]$$

where M_a is the mean molar mass of air, k_a is the thermal conductivity of air, ρ_a is the air density, c_p is the heat capacity of air, and a_T is the thermal accommodation coefficient. For CCN composed of soluble salts and insoluble material, the equilibrium supersaturation of the droplet, S_R^{eq}, is given by Seinfeld and Pandis (1998):

$$S_R^{eq} = \exp\left(\frac{4M_w\sigma}{R_g T \rho_w D_p} - \frac{6n_s M_w}{\pi \rho_w D_p^3}\right) - 1, \quad [10]$$

where σ is the CCN surface tension and n_s is the number of moles of solute per particle.

Gas-Phase Equations

Differential momentum, energy, and mass conservation balances are written for the gas phase assuming a two-dimensional axisymmetric coordinate system. This results in a system of differential equations, each of which is of the general form,

$$\frac{\partial}{\partial t}(r\rho\phi) + \frac{\partial}{\partial z}(r\rho u\phi) + \frac{\partial}{\partial r}(r\rho v\phi) - \frac{\partial}{\partial z}\left(r\Gamma_\phi \frac{\partial \phi}{\partial z}\right) - \frac{\partial}{\partial r}\left(r\Gamma_\phi \frac{\partial \phi}{\partial r}\right) = S_\phi, \quad [11]$$

where r, z are the spatial coordinates, ϕ is the dependent variable (e.g., T, C, u, v), S_ϕ is a source term, and Γ_ϕ is a transport coefficient, both of which depend on the form of ϕ. Table 1 lists the expressions of S_ϕ and Γ_ϕ for each type of ϕ.

The rate of condensation of liquid water (in moles per volume of air per second) on the aerosol particles, J_{cond}, is needed in the water vapor and energy conservation equations. This quantity is given by

$$J_{cond} = \frac{1}{M_w}\frac{dw_L}{dt} \approx \frac{\pi}{2}\frac{\rho_w}{M_w}\sum_{i=1}^{n} N_i D_{pi}^2 \frac{dD_{pi}}{dt}, \quad [12]$$

where w_L is the local liquid water content (kg m^{-3} air) related to the droplet population found in each cell as $w_L \approx \rho_w \frac{\pi}{6}\sum_{i=1}^{n} N_i D_{pi}^3$ (we assume N_i droplets of diameter D_{pi} exist per volume of air, where n is the number of droplet sizes found in the distribution and ρ_w is the density of water). dD_{pi}/dt is calculated from the aerosol growth equations (Equation (7)).

The momentum–equation source term, J_{buoy}, represents the momentum generated from thermal buoyancy effects. For ideal gases it is given by

$$J_{buoy} = -\rho g\left[\frac{T - T_{bulk}(z)}{T_{bulk}(z)}\right], \quad [13]$$

where T is the temperature and g is the component of gravity in the vertical direction. $T_{bulk}(z)$ is the radially-averaged temperature at position z, $T_{bulk}(z) = \frac{\int_0^R 2\pi r T(r,z)dr}{\int_0^R 2\pi r dr}$. Finally, ρ is the gas-phase density, calculated at $T_{bulk}(z)$.

Boundary Conditions of Instrument Model

Two types of inlet velocity conditions are considered: fully developed (i.e., parabolic) or plug flow. The other variables (T, C) are assumed to have a uniform profile at the inlet. At the walls, a no-slip boundary condition is assumed, $u = v = 0$, and for the outlet, $\frac{\partial u}{\partial z} = 0; v = 0$; and $\frac{\partial T}{\partial z} = 0$. A fixed-temperature condition is used for the walls; this is a function of the z-position, and it is computed assuming a linear profile across the conductive tubing. Given that the temperature at the two tips T_c ($r = R$ and $z = 0$), and T_h ($r = R$ and $z = L$) are known, the wall temperature at a given coordinate z is $T_{wall}(z) = T_c + z[T_h - T_c/L]$. At the walls, the air is assumed to be saturated with water vapor at the local temperature and at the outlet, $\frac{\partial C}{\partial z} = 0$. Based on the sheath/aerosol flow ratio, the section of the flow field occupied by the aerosol is calculated from a mass balance. Also, $\frac{\partial u}{\partial r} = \frac{\partial v}{\partial r} = \frac{\partial C}{\partial r} = \frac{\partial T}{\partial r} = 0$ at the symmetry axis and steady- state conditions are assumed. Finally, aerosol particles follow the air flow streamlines with the same velocity as the surrounding air so that sedimentation, coagulation, and Brownian diffusion of particles are neglected.

Numerical Solution of Conservation Equations

The conservation equations cannot be solved analytically, so a numerical solution is obtained from a finite volume discretized procedure (Patankar 1980). A hybrid upwind-central differencing scheme is used for calculating the convective diffusive fluxes over the finite control volumes. The scheme used employs a staggered grid in which each velocity grid node lies between two scalar volumes, ensuring that the calculated pressure field is realistic. The Semi-Implicit Method for Pressure Linked Equations (SIMPLE) iterative solution method (Patankar 1980) is used to solve the hydrodynamic cycle of the discretized momentum equations, while the particle growth equations are solved numerically using the Livermore Solver for ODEs (LSODE) solver of Hindmarsh (1983). The computer code used for the numerical simulations was based on the

TABLE 1
Transfer coefficients and source terms for the gas-phase equations described in the section "Fully-Coupled Instrument Model"

Conservation law	ϕ	Γ_ϕ	S_ϕ
Continuity	1	0	0
z-momentum	u	μ	$-r\frac{\partial P}{\partial \& z}+r\frac{\partial}{\partial \& z}\left(\mu\frac{\partial u}{\partial \& z}\right)+\frac{\partial}{\partial \& r}\left(r\mu\frac{\partial v}{\partial \& z}\right)+J_{buoy}$
r-momentum	v	μ	$-r\frac{\partial P}{\partial \& r}+r\frac{\partial}{\partial \& z}\left(\mu\frac{\partial u}{\partial \& r}\right)+\frac{\partial}{\partial \& r}\left(r\mu\frac{\partial v}{\partial \& r}\right)-\frac{\mu v}{r}$
Heat	T	$\frac{k_a}{c_p}$	$\frac{\Delta H_v}{c_p}J_{cond}$
Water vapor	C	$\rho \& D$	$-\rho J_{cond}$

work of Nenes et al. (2001a). The numerical solution was obtained using 150 cells for each spatial coordinate. The aerosol growth equations use a variable time step, which is scaled to the transit time through a computational cell. The computational grid and time step used ensure that the numerical solution approaches the asymptotic (with respect to grid density) limit.

INSTRUMENT PERFORMANCE AND DESIGN CONSTRAINTS

Effect of Operation and Ambient Conditions on Centerline Supersaturation

The fully-coupled model predictions of centerline supersaturation for variable wall temperature gradient, flow rate, entry temperature, and pressure are shown in Figure 4. Results are shown for the exit supersaturation (defined as $(S_R - 1) \times 100\%$) long after the flows have developed within the instrument. The numerical model predictions suggest that instrument supersaturation responds linearly to changes in flow rate (Figure 4a). This is in agreement with the simple analysis of Equation (6); the numerator is proportional to Q, while the denominator exhibits a much weaker dependence (because $1/\pi\ GQ/\alpha$ ranges typically between 0.1 and 10, which is much smaller than the wall temperature) and thus does not contribute significantly to the supersaturation response. For the same reasons, the wall temperature gradient should yield a proportional response on instrument supersaturation; the full numerical simulations (Figure 4b) confirm this. Predictions of the fully-coupled model suggest that varying the total flow rate and temperature gradient changes supersaturation ca. 0.06% per 100 cm^3 min^{-1} and 0.10% per K m^{-1}, respectively.

Since the instrument operation relies on the difference between heat and mass diffusivity, it is expected that pressure and temperature variations would affect the centerline supersaturation, as both α and D depend on those quantities. The numerical model predictions suggest that instrument supersaturation responds linearly to changes in pressure (Figure 4c), while there is a nonlinear response to changes in entry temperature (Figure 4d). These model trends can again be explained with the simple analysis of Equation (6) after the dependencies of α and D_v on T, P are introduced. If c_p is constant, air behaves like an ideal gas and k is assumed to follow $k = a_1 + a_2 T$,

$$\alpha = \frac{k}{\rho c_p} = \frac{a_1 + a_2 T}{\frac{PM_{air}}{R_g T} c_p} = \frac{T}{P}\left[\frac{R_g a_1}{c_p M_{air}} + \frac{R_g a_2}{c_p M_{air}} T\right]. \quad [14]$$

The diffusivity of water vapor in air is also given by Seinfeld and Pandis (1998),

$$D_v = D_{v,o}\frac{P_o}{P}\left(\frac{T}{T_o}\right)^k, \quad [15]$$

where $k = 1.94$ and $D_{v,o}$ is the value of water vapor diffusivity at a reference temperature T_o and pressure P_o. Substituting Equations (14) and (15) into the $(1/D_v - 1/\alpha)$ term of Equation (6), and assuming that the radial variation of temperature is not significant yields

$$\left(\frac{1}{D_v} - \frac{1}{\alpha}\right) = \left(\frac{P}{T}\right)\left(\frac{T_o^k}{P_o D_o}\frac{1}{T^{k-1}} - \frac{c_p M_w}{R\,(a_1 + a_2 T)}\right). \quad [16]$$

Equation (16) suggests a linear dependence of $S(z)$ on absolute pressure, which is consistent with the fully-coupled simulations. Temperature, however, should exhibit a nonlinear response, which is again seen in the detailed simulations. The difference between α and D_v decrease with increasing T and decreasing P; both trends are consistent with Equation (16) and the fully-coupled model results. The absolute pressure and entrance temperature of the column influence the supersaturation ca. 0.03% per 100 mbar and ca. 0.034% per 10 K, respectively. Small changes in S are thus expected during vertical profiles in airborne measurements. A typical profile may cover a range of ca. 700 mbar, which corresponds to approximately a 0.2% change in S. To maintain a constant S, one may vary other parameters such as the temperature gradient or flow rate to compensate the pressure dependence in S. Such transient corrective algorithms are not included in the current instrument and will be implemented in the future.

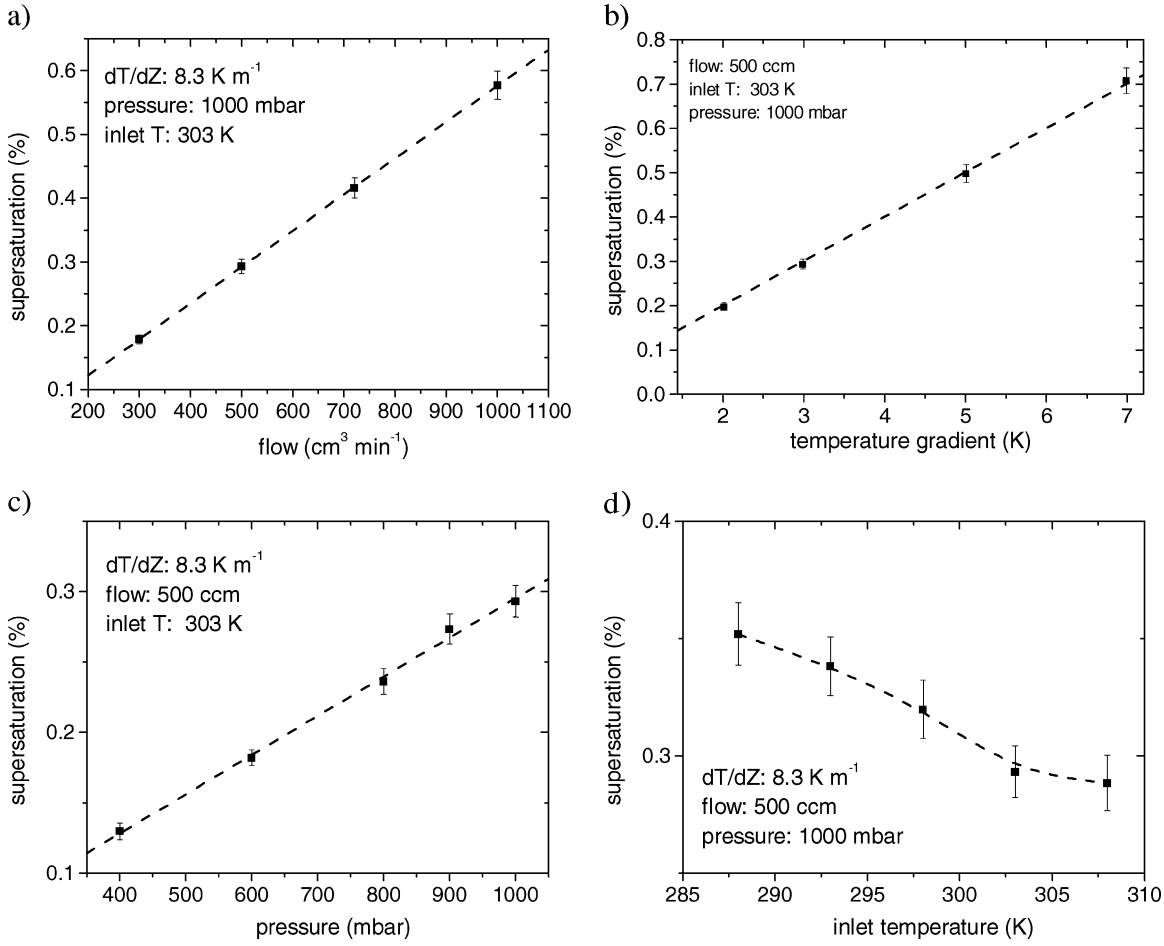

FIG. 4. Predictions of supersaturation based on fully-coupled model simulations for individual variables at conditions similar to normal operation. The error bars on the fully-coupled simulations represent one-sigma variations to the mean centerline supersaturation. Supersaturation is defined as $(S_R - 1) \times 100\%$.

Flow and Streamline Constraints

Before constructing the instrument, extensive simulations using the fully-coupled model (see section "Fully-Coupled Instrument Model" above) placed operational and dimensional constraints on the instrument design (i.e., column dimensions, heating rates, and flow rates). In particular, special attention was devoted to buoyancy related issues that affect the instrument's performance. Large temperature gradients and their associated density variations lead to the development of secondary buoyancy flows that induce undesired pressure gradients and mixing. Consequently, buoyancy flows pose a limit on the maximum temperature gradient that one may use. Earlier attempts by Rogers and Squires (1977) to produce a similar instrument yielded a broad droplet spectrum (compared to that expected when droplets experience the same growth history) because of degraded performance resulting, in part, from a nonlinear temperature profile along the wetted column and potential flow instabilities in certain operating conditions.

Buoyancy effects were evaluated by quantifying the radial change in the streamlines—the maximum amount of change in streamlines perpendicular to the expected flow (Figure 5). For all simulated conditions, there is a notable increase in the deviation of streamlines from straight, laminar flow as the column radius exceeds 12 mm. Flow in the radial direction (induced by convection) near the wetted surface distort diffusional processes and change the centerline supersaturation. As shown by the relatively small influence of flow rate in Figure 5, the column radius is most critical in preventing excessive buoyancy forces. Such effects are expected as the Grashof number (a nondimensional description of buoyancy forces) scales with R^3 and the wall temperature gradient, G. Increasing the flow rate prevents the development of radial flows, but if too fast it may not allow sufficient residence time for growth or even prevent the supersaturation profiles from fully developing. At low supersaturations, low flow rates are necessary to provide the residence time required for activated droplets to grow to a detectable size and also be differentiated from interstitial (i.e., unactivated) particles. However, low flow rates are more susceptible to buoyancy effects and the droplet residence time is ultimately limited by their terminal settling velocity. We operate the CCN instrument

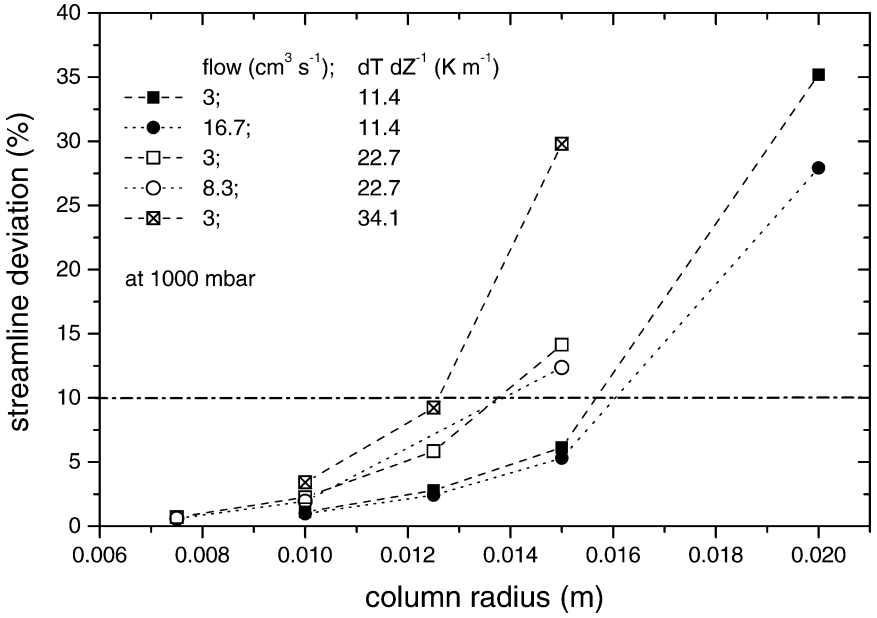

FIG. 5. Model simulations of streamline deviations in the chamber as a function of column radius for a range of flow rates and temperature gradients.

with flow in the downward vertical direction to eliminate problems associated with the suspension of larger droplets in the sample flow. Heating rates greater than 34.1 K m^{-1} are acceptable (Figure 5); however, our design avoids flow reversal for temperature gradients of 15 K m^{-1} at a flow rate of 11 min^{-1}, which corresponds to a supersaturation of ca. 3% and is sufficiently high for ambient measurements.

Optical Detection Constraints

For the measurement to be quantitative, all particles above the detection threshold must correspond to activated droplets. When measuring CCN at supersaturation levels greater than 0.2%, interstitial (i.e., unactivated) aerosol is smaller than the 1 μm threshold. However, as the instrument supersaturation decreases, there is a risk of miscounting droplet concentrations, as the equilibrium size of interstitials can exceed the detection threshold size. Using Köhler theory for calculating interstitial equilibrium size, the lowest limit in supersaturation for a 1 μm threshold is 0.13% for $(NH_4)_2SO_4$ aerosol and 0.2% for a hydrophilic insoluble particle. Therefore, to obtain measurements of CCN at lower supersaturations, the threshold size must be increased. This is important, as simulations suggest that the instrument is capable of producing supersaturations less than 0.1%.

Although increasing the threshold detection size, $D_p{}^o$, improves the instrument dynamic range, the residence time for growth, $\tau_{Rg} = \pi R^2 L_g/Q$, where L_g is the length of the chamber available for growth (i.e., where the fields are developed), imposes an upper limit on $D_p{}^o$ because droplets need a finite time, τ_g, to grow to the threshold size. A rough estimate of τ_g, can be determined from Equation (7); neglecting curvature and solute effects,

$$\frac{dD_p}{dt} = \frac{GS}{D_p}, \qquad [17]$$

where $G = \rho_w R_g T/4P^o_{H_2O} D'_v M_w + \Delta H_v \rho_w/4k'_a T(\Delta H_v \rho_w/TR_g - 1) \approx const$. Assuming that the inlet size of the CCN is D^i_p, and that growth is experienced only when the supersaturation profile is developed (a reasonable assumption if the entry length is small compared to the total tube length), then Equation (17) can be integrated to yield the size of the droplet when it reaches the OPC:

$$D^o_p = \left(D^i_p + 2GS\tau_g\right)^{1/2}. \qquad [18]$$

Since D^o_p must be at least equal to the threshold droplet detection size, then the minimum τ_g is:

$$\tau_g = \frac{\left(D^o_p\right)^2 - \left(D^i_p\right)^2}{2GS}. \qquad [19]$$

Equation (19) illustrates why τ_g increases when the instrument S is lowered: (1) the driving force for growth (S) decreases, and (2) $D_p{}^o$ increases so that interstitial aerosol can be distinguished from activated CCN (i.e., because D_{pc} increases). One must note that as a consequence of Köhler theory, $D_p{}^i$ also increases with decreasing S; this effect, which tends to decrease τ_g, is rather small.

The combination of the growth and residence timescales (i.e., $\tau_{Rg} > \tau_g$) yields a criterion that ensures the detectability

of droplets in the instrument,

$$\frac{2\pi R^2 L_g G S}{Q\left[\left(D_p^o\right)^2 - \left(D_p^i\right)^2\right]} < 1. \qquad [20]$$

INSTRUMENT EVALUATION

Monodisperse Aerosols

The principle of the new CCN instrument was validated by activating laboratory generated aerosol of known composition and comparing measurements to Köhler theory. Each experiment is carried out by keeping the instrument supersaturation fixed and measuring the degree of activation when changing the inlet particle size. Monodisperse aerosol is produced by nebulizing a $(NH_4)_2SO_4$ solution, which is subsequently dried, charged, and classified by a differential mobility analyzer (DMA; TSI 3081). The classified aerosol size is controlled by varying the flow rates and electric field within the DMA. A mixing volume at the outlet of the DMA uniformly distributes the aerosol, which is simultaneously sampled by a scanning mobility particle sizer (SMPS; TSI 3081), a condensation particle counter (CPC; TSI 3010) and the streamwise CCN instrument. The SMPS confirms the monodisperse output of the first DMA and quantifies the amount of multiple charged particles (Figure 6); the latter become important when large particles are classified. Several scans (1 min each) of the size distribution are obtained for each monodisperse output to ensure reproducibility during the calibration. Figure 6 illustrates a series of monodisperse distributions during a calibration cycle, which includes 20 DMA-selected sizes and 3 scans at each size. After selecting a new median size from the DMA, the mixing volume requires less than a minute to equilibrate; consequently, the first scan of a new size is omitted in the analysis. The remaining scans are averaged and the median diameter of the distribution determines the dry particle size for the calibration. The integrated droplet distribution from the SMPS yields the total aerosol concentration and is generally within 30% of the CPC measurements. The SMPS concentrations are normalized to the average number concentrations recorded by the CPC for the same scan period. Number and droplet concentrations are recorded every second by the CPC and CCN, respectively, and range between zero and 10^4 particles cm^{-3}. The CPC counter has detection efficiency near 100% for particles with diameters larger than 0.018 μm and is used as a reference for comparing the activated fraction of CCN to total aerosol concentration. The median diameter of the monodisperse size distribution that activates 50% of the aerosol to CCN is used to calculate the corresponding supersaturation of the CCN instrument using Köhler theory (assuming a van't Hoff factor of 3).

The instrument yields sharp activation curves (Figure 6), and verifies the novel technique of generating a supersaturation profile. Several experiments at different operating conditions (i.e., different flow rates and temperature gradients) were performed to assess the overall performance of the instrument (Figure 6). These experiments were performed at ambient pressure (ca. 1000 mbar) and temperature (ca. 298 K). The entrance of the wetted column was heated to 302 K. At a flow rate of 500 cm^3 min^{-1} and measured temperature difference between the ends of the column of 5 K, a sharp rise in the activated droplet concentration occurred at a mediam diameter of 68.0 nm. Using Köhler theory for $(NH_4)_2SO_4$ aerosol, the corresponding critical supersaturation of 68.0 nm diameter particles is 0.26%, which we also infer to be the centerline supersaturation of the column. Model simulations suggest that a temperature difference of 5 K should yield ca. 0.4% supersaturation; however, these calculations do not account for the insulating effects of the filter paper and the placement of the temperature probes in the original design. Thus, the nominal temperature difference does not reflect the actual temperatures at the wetted surface facing the flow. For the model predictions to match the inferred supersaturation, the effective temperature difference between inlet and outlet shoud be about 2.5 K, or 50% of the nominal difference of 5 K. This decrease in effective temperature difference is an inherent feature to any CCN instrument (e.g., Chuang et al. 2000; Nenes et al. 2001a). For a 2.5 K nominal temperature difference and a 50% effective temperature drop across the filter paper, the model predicts a supersaturation of about 0.1%, which is very close to the 0.09% inferred by the calibration (Figure 6). In the current design, we have reduced this temperature difference between model and experimental results by changing the temperature probes and using a porous, conductive wetting material.

For reduced flow (i.e., 300 cm^3 min^{-1}) and a 5 K nominal temperature difference, a sharp rise in the activated droplet concentration occurred at a median diameter of 129 nm. In light of the discussion from the section, "Flow and Streamline Constraints" above, 129 nm particles have a critical diameter of 1.5 μm, which is above the 1 μm diameter threshold for defining CCN. Hence, to characterize activated CCN for particles associated with lower supersaturations, the detection size must be increased accordingly, and the configuration of the instrument must be modified to allow for longer residence time in the column (either by extending the column and/or reducing the flow rate). Although three of the growth curves in Figure 6 represent droplet growth for aerosol below the nominal minimum supersaturation of the instrument, the sharp curves illustrate the instrument's ability to detect and measure droplet growth. The model predicts that the effective temperature difference should be 1.75 K (0.1% supersaturation) if the nominal value is set to 5 K at 300 cm^3 min^{-1}, for a 2.5 K nominal temperature difference and a 65% effective temperature drop across the filter paper, the model predicts a supersaturation of about 0.05%, which is close to the 0.06% inferred by the calibration (Figure 6). It should be noted, however, that at this very low supersaturation level using a 1 μm cutoff diameter for the droplet detection may not

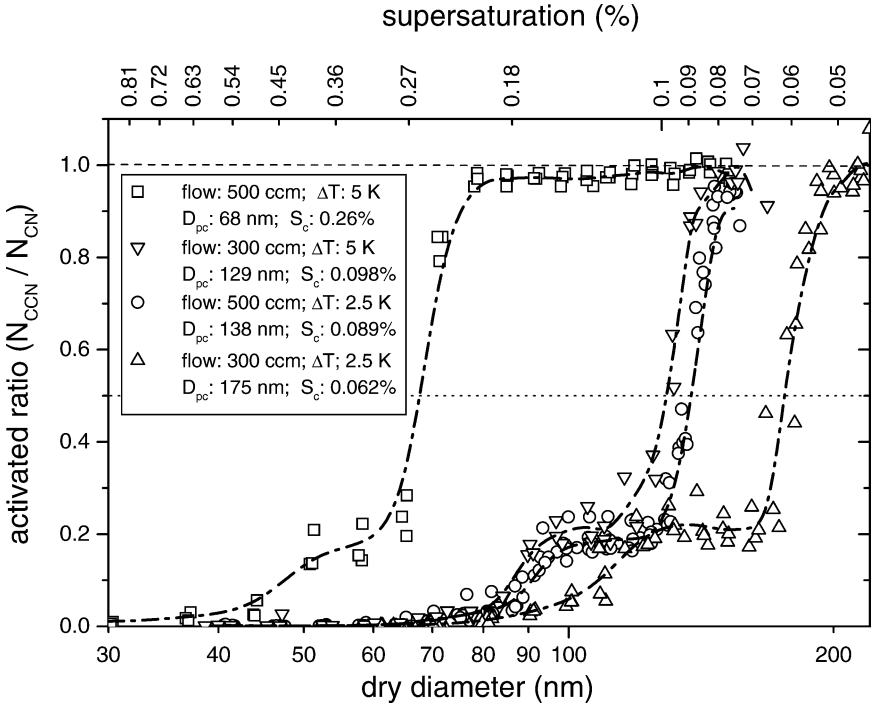

FIG. 6. Calibration and growth curves of CCN at different operating conditions. The dry diameters are based on median diameters from Figure 6. Aerosol at a particular dry diameter is considered activated when the ratio of CCN (i.e., droplets greater than 1 μm) to total aerosol is greater than 0.5. The shoulders result from multiple charge particles from the DMA classification.

be sufficient to differentiate interstitial from activated droplets (see section "Optical Detection Constraints" above).

Polydisperse Aerosols

Ambient aerosol are polydisperse, and their concentration varies orders of magnitude—from more than 10^3 cm^{-3} (e.g., Herrerra and Castro 1988) to fewer than 10 cm^{-3} (e.g., Radke and Hobbs 1969); the instrument should perform well for this wide range of aerosol conditions. To test the performance of the instrument at a range of concentrations of a known number of CCN, we produced broad aerosol distributions to approximate ambient number distributions using a $(NH_4)_2SO_4$ aerosol. The setup was similar to the setup in the preceding section; however, the ratio of flow rates on the DMA was changed to yield a broad size distribution (i.e., using a flow ratio of nearly 2 to 1 for sheath and aerosol flows in the DMA). The polydisperse tests described here were performed at the same supersaturation with $(NH_4)_2SO_4$ aerosol. Four size distributions were selected (Figure 7) with median diameters of ca. 48, 65, 83, and 100 nm. By producing broad distributions of a known composition (i.e., $(NH_4)_2SO_4$), we verify the performance of the CCN instrument. In the monodisperse calibration (see the preceding section), we determined that the supersaturation of the instrument operating at a flow rate of 500 cm^3 min^{-1} with a measured temperature difference of 5 K yielded a sharp cutoff at 68.0 nm (0.26% S). Extending the results from this calibration, the dashed line in Figure 7 shows the critical size for the given operating conditions. Figure 7 shows the interscan variability, which was small for most of the scans. By integrating each of the number distributions for particle diameters greater than the critical diameter, we obtain the expected CCN concentrations. Figure 8 shows a strong 1:1 relationship between the expected and measured CCN concentrations ($r^2 = 0.81$; n = 26). For 65 nm particles, for example, there are CCN predictions at 6 sizes from 300 to 9000 cm^{-3}. The number concentration decreases with time as the impactor in front of the classifying DMA gradually collects aerosol and increases its efficiency as a filter. At smaller concentrations, the size distributions were not as reproducible and introduced significant errors in the expected CCN concentrations. There variations are especially noticeable for size distributions centered at 65 nm and near the critical diameter of 68 nm. If these outliers are removed, the correlation improves to $r^2 = 0.998$. No significant rolloff from coincidence losses was observed until droplet concentrations exceeded 8000 cm^{-3}, and these might be easily addressed by increasing the sheath-to-aerosol ratio.

SUMMARY

To address the need for fast and high-quality CCN measurements, we have developed an instrument that employs a simple yet robust method of precisely generating a supersaturation within a axisymmetric flow geometry. By maintaining a

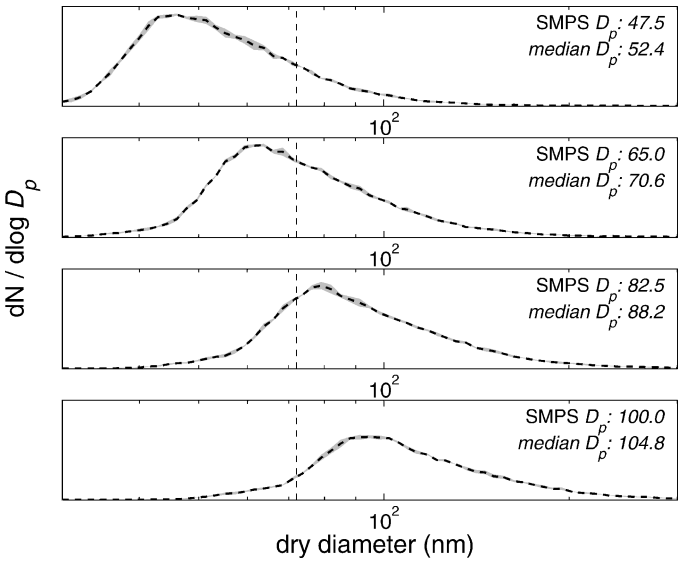

FIG. 7. Polydisperse dry aerosol distributions of $(NH_4)_2SO_4$. The vertical dashed line shows the calibrated critical diameter at 500 cm^3 min^{-1} and a measured temperature gradient of 5 K. Particle sizes larger than the vertical dashed line are expected to be CCN active. The actual values of the verticalaxis are not shown because they change after each cycle.

constant wall temperature gradient along the flow direction, differences in thermal and water vapor diffusivity establish a quasi-uniform supersaturation at each flow streamline. The main features of this instrument are as follows:

- Continuous flow allows fast sampling (at least 1 sample per second), which is suitable for airborne measurements.
- Supersaturation along a streamline is nearly constant. The maximum supersaturation is located at the centerline, which maximizes droplet growth.
- Supersaturation is a function of flow rate, pressure, and temperature, and it can be easily controlled and maintained.
- Axisymmetric geometry reduces buoyancy effects and thus size (because lower flow rates can be used).
- The same supersaturation can be generated from different combinations of wall temperature gradients and flow rates.

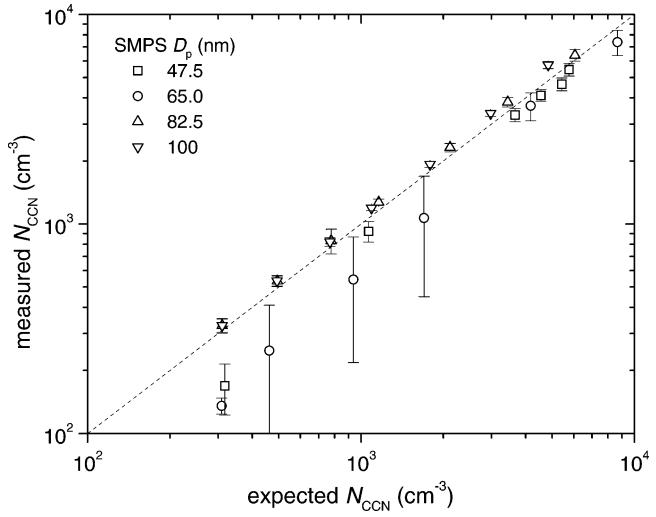

FIG. 8. Measured versus calculated CCN concentration using the polydisperse dry aerosol distributions of known composition. SMPS D_p represents the desired diameter of each polydisperse size distribution. Actual median diameters were calculated during analysis.

The principle of the CCN chamber has been validated by controlled laboratory experiments and independent closure measurements. The calibration of the CCN instrument yields a sharp activation curve using monodisperse aerosol of known composition, such as ammonium sulfate, and it agrees well with theoretical predictions based on Köhler theory. The operating range of the CCN instrument, based on the current configuration, is between 0.13 and 3% supersaturation. The lower limit is controlled by the 1 μm threshold in the droplet detection, since lower supersaturations would result in counting biases. The upper limit is constrained by the development of secondary flows from thermal buoyancy effects at sample flows of 1 lpm. Simulations indicate that much lower supersaturations can be measured with modest modifications to the flow chamber. By maintaining a quasi-uniform supersaturation along the flow axis, our design minimizes measurement uncertainty related to different droplet growth times.

Although the full potential of the new design has yet to be explored, the value of this research tool for studying aerosol–cloud interactions has already been demonstrated (e.g., VanReken et al. 2003). It is clear that the unparalleled flexibility in controlling supersaturation together with the simplicity and compactness of the design provides a much-needed methodology for routine CCN measurements.

NOMENCLATURE

a_c	condensation coefficient
a_T	thermal accommodation coefficient
C	water vapor concentration
c_p	heat capacity of air
D_p	droplet diameter
D'_v, D_v, $D_{v,o}$	diffusivity of water vapor in air
G	wall temperature gradient
J_{bouy}	momentum from thermal buoyancy effects
J_{cond}	rate of condensation of liquid water
k_a, k'_a	thermal conductivity of air
M_a	mean molar mass of air
M_w	molar mass of water
N	droplet concentration
n_s	moles of solute per particle
P	ambient pressure
$P^o_{H_2O}$	equilibrium water vapor pressure

P_{H_2O}	partial pressure of water vapor
Q	air flow rate
R	column radius
r, z	radial and axial coordinates
R_g	universal gas constant
S_R^{eq}	equilibrium supersaturation ratio
S_ϕ	source term (Table 1)
S_R	saturation ratio
S	Supersaturation, S_R-1
T	temperature
T_{bulk}	radially averaged temperature
T_o, P_o	reference temperature and pressure
u, v	air velocity in radial and axial directions
V	average air velocity
w_L	liquid water content
x_C	distance of water vapor propagation
x_T	distance of heat propagation

Greek Letters

α	diffusivity of heat
ΔH_v	enthalpy of evaporation
ϕ	dependent variable (Table 1)
Γ_ϕ	transport coefficient (Table 1)
ρ_a	density of air
ρ_w	water density
σ	CCN surface tension
τ_C	timescale of water vapor transfer to centerline
τ_T	timescale for heat transfer to centerline

REFERENCES

Albrecht, B. A. (1989). Aerosols, Cloud Microphysics, and Fractional Cloudiness, *Science* 245:1227–1230.

Bartlett, B. M., and Ayers, G. P. (1981). Static Diffusion Cloud Chamber, *J. Rech. Atmos.* 15:231–233.

Charlson, R. J., Schwartz, S. E., Hales, J. M., Cess, R. D., Coakley, J. A., Hansen, J. E., and Hofmann, D. J. (1992). Climate Forcing by Anthropogenic Aerosols, Science 255:423–430.

Chuang, P., Smith, J., Flagan, R., and Seinfeld, J. (2000). Design of a CCN Instrument for Airborne Measurement, *J. Atmos. Sci. Technol.* 17:1005–1019.

Chuang, P. Y. (2003). Measurement of the Timescale of Hygroscopic Growth for Atmospheric Aerosols, *J. Geophys. Res.* 108 (Art. No. 4282).

Delene, D. J., Deshler, T., Wechsler, P., and Vali, G. A. (1998). A Balloon-borne Cloud Condensation Nuclei Counter, *J. Geophys. Res.* 103:8927.

Facchini, M., Decesari, S., Mircea, M., Fuzzi, S., and Loglio, G. (2000). Surface Tension of Atmospheric Wet Aerosol and Cloud/Fog Droplets in Relation to Their Organic Carbon Content and Chemical Composition, *Atmos. Environ.* 34:4853–4857.

Facchini, M. C., Mircea, M., Fuzzi, S., and Charlson, R. J. (1999). Cloud Albedo Enhancement by Surface-active Organic Solutes in Growing Droplets, *Nature* 401:257–259.

Feingold, G., and Chuang, P. Y. (2002). Analysis of the Influence of Film-forming Compounds on Droplet Growth: Implications for Cloud Microphysical Processes and Climate, *J. Atmos. Sci.* 59:2006–2018.

Fukuta, N., and Saxena, V. (1979). A Horizontal Thermal Gradient Cloud Condensation Nucleus Spectrometer, *J. Appl. Meteor.* 18:1352–1362.

Fukuta, N., and Walter, L. (1970). Kinetics of Hydrometer Growth from the Vapor Spherical Model, *J. Atmos. Sci.* 27:1160–1172.

Hegg, D., Gao, S., Hoppel, W., Frick, G., Caffrey, P., Leaitch, W., Shantz, N., Ambrusko, J., and Albrechcinski, T. (2001). Laboratory Studies of the Efficiency of Selected Organic Aerosols as CCN, *Atmos. Res.* 58:155–166.

Herrerra, J. R., and Castro, J. J. (1988). Production of Cloud Condensation Nuclei in Mexico City, *J. Appl. Meteor.* 27:1189–1192.

Hindmarsh, A. (1983) ODEPACK: A systematized collection of ODE solvers, in Scientific Computing, edited by Stepleman et al., and North-Holland. New York 55–64.

Hoppel, W., Twomey, S., and Wojciechowski, T. (1979). A Segmented Thermal Diffusion Chamber for Continuous Measurements of CN, *J. Aerosol Sci.* 10:369–373.

Houghton, J., Ding, Y., Griggs, D., Noguer, M., van der Linden, P., Dai, X., Maskell, K., and Johnson, C. (2001) Climate Change, 2001: The Science of Climate Change, Cambridge University Press. New York, Cambridge, UK.

Hudson, J. G. (1989). An Instantaneous CCN Spectrometer, *J. Atmos. Oceanic Technol.*, 6:1055–1065.

Incropera, F., and DeWitt, D. (1990) *Fundamentals of Heat and Mass Transfer*, (John Wiley & Sons). New York, .

Kaufman, Y., Hobbs, P., Kirchhoff, V., Artaxo, P., Remer, L., Holben, B., King, M., Ward, D., Prins, E., Longo, L., Mattos, L., Nobre, C., Spinhirne, J., Ji, Q., Thompson, A., Gleason, J., Christopher, S., and Tsay, S. (1998). Smoke, Clouds, and Radiation—Brazil (SCAR-B) Experiment, *J. Geophys. Res.* 103:31783–31808.

Köhler, H. (1936). The Nucleus in and the Growth of Hygroscopic Droplets, *Trans. Faraday Soc.* 32:1152–1161.

Laaksonen, A., Korhonen, P., Kulmala, M., and Charlson, R. (1998). Modification of the Kuhler Equation to Include Soluble Trace Gases and Slightly Soluble Substances, *J. Atmos. Sci.* 55:853–862.

Lala, G. G., and Jiusto, J. E. (1977). An Automatic Light Scattering CCN Counter, *J. Appl. Meteor.* 16:413–418.

Mircea, M., Facchini, M., cDecesari, S., Fuzzi, S., and Charlson, R. (2002). The Influence of the Organic Aerosol Component on CCN Supersaturation Spectra for Different Aerosol Types, *Tellus* 54:74–81.

Nenes, A., Charlson, R., Facchini, M., Kulmala, M., Laaksonen, A., and Seinfeld, J. (2002). Can Chemical Effects on Cloud Droplet Number Rival the First Indirect Effect?, *Geophys. Res. Lett.* 29. (Art. No. 1848).

Nenes, A., Chuang, P., Flagan, R., and Seinfeld, J. (2001a). A Theoretical Analysis of Cloud Condensation Nucleus (CCN) Instruments, *J. Geophys. Res.* 106:3449–3474.

Nenes, A., Ghan, S., Abdul-Razzak, H., Chuang, P. Y., and Seinfeld, J. H. (2001b). Kinetic: Limitations on Cloud Droplet Formation and Impact on Cloud Albedo, *Tellus* 53:133–149.

Oliveira, J. C. P., and Vali, G. (1995). Calibration of a Photoelectric Cloud Condensation Nucleus Chamber, *Atmos. Res.* 38:237.

Patankar, S. (1980) (Numerical Heat Transfer and Fluid Flow), McGraw-Hill. New York, .

Pruppacher, H. R., and Klett, J. D. (1997) Microphysics of Clouds and Precipitation, Kluwer Academic Publishers. New York, .

Radke, L. F., and Hobbs, V. P. (1969). Measurement of Cloud Condensation Nuclei, Light Scattering Coefficient, Sodium-containing Particles, and Aitken Nuclei in the Olympic Mountains of Washington, *J. Atmos. Sci.* 26:281.

Raes, F., Bates, T., McGovern, F., and VanLiedekerke, M. (2000). The 2nd Aerosol Characterization Experiment (ACE-2): General Overview and Main Results, *Tellus* 52:111–125.

Ramanathan, V., Crutzen, P., Lelieveld, J., Mitra, A., Althausen, D., Anderson, J., Andreae, M., Cantrell, W., Cass, G., Chung, C., Clarke, A., Coakley, J., Collins, W., Conant, W., Dulac, F., Heintzenberg, J., Heymsfield, A., Holben, B., Howell, S., Hudson, J., Jayaraman, A., Kiehl, J., Krishnamurti, T., Lubin, D., McFarquhar, G., Novakov, T., Ogren, J., Podgorny, I., Prather, K., Priestley, K., Prospero, J., Quinn, P., Rajeev, K., Rasch, P., Rupert, S., Sadourny,

R., Satheesh, S., Shaw, G., Sheridan, P., and Valero, F. (2001). Indian Ocean Experiment: An Integrated Analysis of the Climate Forcing and Effects of the Great Indo-Asian Haze, *J. Geophys. Res.* 28371–28398.

Rogers, C., and Squires, P. (1977) A new device for studies of cloud condensation nuclei active at low supersaturations, in Ninth International Conference on Atmospheric Aerosols, Condensation, and Ice Nuclei, edited by A. Roddy , and T. O'Conner Galway University Press, University College. Boston, Ireland.

Rosenfeld, D. (1999). TRMM Observed First Direct Evidence of Smoke from Forest Fires Inhibiting Rainfall, *Geophys. Res. Lett.* 26:3105–3108.

Seinfeld, J. H., and Pandis, S. N. (1998).. Atmospheric Chemistry and Physics: From Air Pollution to Climate Change, John Wiley, New York.

Shantz, N. C., Leaitch,N., and Caffrey, P. F. (2003). Effect of Organics of Low Solubility on the Growth Rate of Cloud Droplets, *J. Geophys. Res.* 108. (Art. No. 4168).

Shulman, M. L., Jacobson, M. C., Charlson, R. J., Synovec, R. E., and Young, T. E. (1996). Dissolution Behavior and Surface Tension Effects of Organic Compounds in Nucleating Cloud Droplets, *Geophys. Res. Lett.* 23:277–280.

Sinnarwalla, A., and Alofs, D. (1973). A Cloud Nucleus Counter with Long Available Growth Time, *J. Appl. Meteor.* 12:831–835.

Twomey, S. (1963). Measurements of Natural Cloud Nuclei, *J. Rech. Atmos.* 1:101–105.

Twomey, S. (1977). The Influence of Pollution on the Short-wave Albedo of Clouds, *J. Atmos. Sci.* 34:1149–1152.

Twomey, S., and Wojciechowski, T. A. (1969). Observations of the Geographical Variations of Cloud Nuclei, *J. Atmos. Sci.* 25:333–334.

VanReken, T. M., Rissman, T. A., Roberts, G. C., Varutbangkul, V., Jonsson, H. H., Flagan, R. C., and Seinfeld, J. H. (2003). Toward Aerosol/Cloud Condensation Nuclei (CCN) Closure During CRYSTAL-FACE, *J. Geophys. Res.* 108. (Art. No. 4633).